16 May 2024

ALMA MATER STUDIORUM
UNIVERSITÀ DI BOLOGNA

ARCHIVIO ISTITUZIONALE
DELLA RICERCA

Alma Mater Studiorum Università di Bologna
Archivio istituzionale della ricerca

Characterizing hydrogen and tetrel bonds in clusters of CO2with carboxylic acids

This is the final peer-reviewed author's accepted manuscript (postprint) of the following publication:

*Published Version:*
Characterizing hydrogen and tetrel bonds in clusters of CO2with carboxylic acids / Li W.; Melandri S.; Evangelisti L.; Calabrese C.; Vigorito A.; Maris A.. - In: PHYSICAL CHEMISTRY CHEMICAL PHYSICS. - ISSN 1463-9076. - STAMPA. - 23:31(2021), pp. 16915-16922. [10.1039/d1cp02568f]

This version is available at: https://hdl.handle.net/11585/853163 since: 2022-02-04

*Published:*

DOI: http://doi.org/10.1039/d1cp02568f

*Terms of use:*

Some rights reserved. The terms and conditions for the reuse of this version of the manuscript are specified in the publishing policy. For all terms of use and more information see the publisher's website.

(Article begins on next page)

This item was downloaded from IRIS Università di Bologna (https://cris.unibo.it/).
When citing, please refer to the published version.

This is the final peer-reviewed accepted manuscript of:

Li, Weixing, Sonia Melandri, Luca Evangelisti, Camilla Calabrese, Annalisa Vigorito, and Assimo Maris. "Characterizing hydrogen and tetrel bonds in clusters of $CO_2$ with carboxylic acids." Physical Chemistry Chemical Physics 23, no. 31 (2021): 16915-16922.

The final published version is available online at: https://doi.org/10.1039/D1CP02568F

Rights / License:

The terms and conditions for the reuse of this version of the manuscript are specified in the publishing policy. For all terms of use and more information see the publisher's website.

*This item was downloaded from IRIS Università di Bologna (https://cris.unibo.it/)*

***When citing, please refer to the published version.***

# Characterizing hydrogen and tetrel bonds in clusters of $CO_2$ with carboxylic acids†

Weixing Li, ‡ Sonia Melandri, Luca Evangelisti, Camilla Calabrese, § Annalisa Vigorito and Assimo Maris *

The interaction between carbon dioxide and planar carboxylic acids has been investigated through the analysis of the microwave spectrum of the acrylic acid·$CO_2$ complex and quantum chemical modeling of the R–COOH·$(CO_2)_{1,16}$ clusters, where R = H, $CH_2CH$. As regards the 1 : 1 compounds, two species, involving the s-*cis* and s-*trans* conformers of acrylic acid were observed. For both of them, a similar bidentate interaction arises between the carbonyl group of $CO_2$ and the carboxylic group of the organic acid, leading to the formation of a planar six-membered ring. The binding energy is estimated to be $D_e \simeq 21$ kJ mol$^{-1}$, 1/3 being the energy contributions of the tetrel to hydrogen bonds, respectively. In the 1 : 16 clusters, the ring arrangement is broken, allowing for the interaction of the acid with several $CO_2$ molecules. The $CO_2$ molecules completely surround formic acid, whereas, in the case of acrylic acid, they tend to avoid the allyl chain.

Carbon dioxide is a naturally occurring compound, which is formed in combustion, decomposition and respiratory processes and converted to carbohydrates by photosynthesis. $CO_2$ plays an essential role as a greenhouse gas in the Earth's atmosphere, and it is the main component of Mars' and Venus' atmospheres. Moreover, $CO_2$ spans a wide variety of physical and chemical applications, depending on its state. For example, in the gas form, $CO_2$ constitutes the active material of powerful lasers, while in its solid form (m.p. 216.6 K) it is used both as a refrigerant and an abrasive. In its supercritical fluidic form ($scCO_2$), it plays an important role as green solvent, due to its low toxicity and environmental impact.[1,2] In the last century, the greatest $CO_2$ emissions have been of anthropogenic origin, leading to an ever growing concentration level in the atmosphere, which is related to the increasing global warming and the acidification of oceans. In order to contain these effects, strategies aimed to the capture and storage of $CO_2$ are widely studied.[3] In this context, acquiring knowledge on how $CO_2$ interacts with the surroundings is necessary to understand the physicochemical properties leading both the adsorption processes, exploited in sequestration of waste $CO_2$, and the solvation properties, which can explain the behaviour of $scCO_2$.

As regards the gas phase, high resolution rotational spectroscopy coupled to computational modeling is a powerful strategy to determine the structural and energetic characteristics of the interacting moieties.[4] This synergic approach is able to determine the behaviour of an apolar probe like $CO_2$, with respect to the binding abilities of its oxygens and carbon atoms of acting as proton and electron acceptor, respectively.

$CO_2$ acts as a proton acceptor forming linear complexes when interacting with strong hydracids (HF[5] and HCl[6]) whereas it acts as a Lewis acid, forming T-shaped complexes, in the case of water,[7] hydrobromic acid,[8] dimethylether,[9] $N_2$,[10] pyridine,[11] and cyanoacetylene.[12] Interestingly, both behaviors were evidenced in the case of HCN·$CO_2$, where a linear[13] and a T-shaped[14] isomer were detected, the latter being the most stable, and in the $(H_2O)_2$·$CO_2$ trimer,[15] where $CO_2$ acts as a proton donor towards a water molecule and as a proton acceptor with respect to the other water molecule forming a cyclical structure.[15] The simultaneous interaction of both the carbon and oxygen atoms of $CO_2$ has been recognized also in other $CO_2$ complexes, such as those with carbonyl sulfide,[16,17] formaldehyde,[18] methanol,[19] propylene oxide,[20] ethylene oxide,[21] difluoromethane,[22] formic acid (FA),[23] 1,1-difluoroethylene,[24] trifluoroethylene,[25] formamide,[26] isopropylamine,[27] and 2-methoxypyridine.[28] In the latter, the two observed forms of the complex are stabilized by three intermolecular bonds involving all $CO_2$ constituting atoms. A recent study on

*Dipartimento di Chimica "G. Ciamician", Università di Bologna, via Selmi 2, I-40126 Bologna, Italy. E-mail: assimo.maris@unibo.it; Tel: +39 051 2099502*

† Electronic supplementary information (ESI) available: Theoretical Cartesian structures of the global minima of the clusters: FA·$(CO_2)_{16}$ (FA_16CO2_GM.xyz), *c*AA·$(CO_2)_{16}$ (*c*AA_16CO2_GM.xyz), and *t*AA·$(CO_2)_{16}$ (*t*AA_16CO2_GM.xyz). See DOI: 10.1039/d1cp02568f

‡ Present address: Department of Chemistry, Fudan University, Shanghai 200438, China.

§ Present address: Departamento de Química Física, Universidad del País Vasco (UPV/EHU), Apartado 644, E-48080 Bilbao, Spain. Biofisika Institute (CSIC, UPV/EHU), Barrio Sarriena, S/N, E-48940, Spain. Fundación Biofisika Bizkaia/Biofisika Bizkaia Fundazioa (FBB), Barrio Sarriena, S/N, E-48940, Spain.

chlorotrifluoromethane·$CO_2$, evidenced that in the most stable structure the $CO_2$ moiety is almost parallel to the $C_{3v}$ symmetry axis of $CF_3Cl$, with two fluorine atoms pointing toward one of its oxygen atoms in a bifurcated arrangement and the chlorine atom faced to the $CO_2$ carbon atom.[29]

Comparison of the intermolecular distances and the binding energies values indicates that $CO_2$ forms the stronger linkages with acids. Focusing on the carboxylic acids, only data on the 1 : 1 adduct with the smallest one (FA),[23] are available. With FA, $CO_2$ acts both as a proton and electron acceptor, forming a primary $OH_{FA}\cdots O_{CO_2}$ interaction and a secondary $O_{FA}\cdots C_{CO_2}$ link, giving rise to a planar six-membered ring arrangement.

In order to find out how the increased molecular complexity of the carboxylic acid partner affects the binding properties of $CO_2$, we have undertaken the study of the $CO_2$ complex with acrylic acid (AA). AA is the simplest unsaturated carboxylic acid, and previous rotational spectroscopy studies[30–32] showed that it is planar. In particular, two nearly isoenergetics conformers exist, namely s-*cis*-AA (*c*AA) and s-*trans*-AA (*t*AA), *c*AA being more stable than *t*AA by about 0.7 kJ $mol^{-1}$.[30] They form strong dimers with each other,[33] and with other carboxylic acids.[34–37]

On the other hand, the effectiveness of $CO_2$ as solvent is not fully understood and one of the main reasons is the difficulty of an accurate theoretical description of the phenomenon. A step by step approach starting from the study of small systems to be taken as models to benchmark theoretical calculations can be of great help in undertaking the study of larger systems. In this work we have a double objective: to study the acid·$CO_2$ model system and once the analysis protocol has been developed, extend it to the nanosolvation of the acid to observe the changes in the molecular interactions. We report here the rotational spectrum of AA·$CO_2$ in the frequency range 6.5–18.5 GHz and guided by the spectroscopic evidence, we employ quantum chemical tools to predict the behaviour of AA·$(CO_2)_{16}$ and FA·$(CO_2)_{16}$ clusters.

## 2 Experimental methods

$CO_2$ diluted in helium with a proportion of about 1% at a stagnation pressure of 0.3 MPa was passed over a container with AA (commercial sample) kept at room temperature and expanded through a solenoid valve (General Valve, Series 9, nozzle diameter 0.5 mm) into the Fabry–Pérot cavity. Gas phase molecules were generated in supersonic expansion conditions in which the molecules reach very low rotational temperatures and the most stable forms are trapped in their energy minima. Details of the used pulsed jet Fourier transform microwave spectrometer (COBRA-type),[38,39] which covers the range 6.5–18.5 GHz, have been described previously.[40] The spectral line positions were determined after Fourier transformation of the time-domain signal with 8k data points, recorded with 100 ns sample intervals. Each rotational transition appears as a doublet due to the Doppler Effect. The line position is calculated as the arithmetic mean of the frequencies of the Doppler components. The estimated accuracy of the frequency measurements is better than 3 kHz. Lines separated by more than 7 kHz are resolvable. Rotational transition lines were fitted using the CALPGM program suite,[41] using the Watson *S*-reduction and $I^r$ representation.[42]

## 3 Computational methods

The automatized exploration of the chemical structure space was performed using the free open source Grimme's Conformer–Rotamer Ensemble Sampling Tool (CREST-2.9).[43] This program generates the rotamers by extensive MeTaDynamic sampling end (iMTD algorithm), and optimizes their geometry by a semi-empirical density functional based Tight-Binding method (xTB-6.2.3).[44] Different options are available for single molecules or molecular aggregates. In the first case a genetic *Z*-matrix crossing step is introduced at the end of the meta-dynamics, whereas in the latter case reduced settings are used and an ellipsoid wall potential is automatically determined and added to the meta-dynamics. In the present work the GFN2-xTB level of theory was applied to characterize molecular aggregates.

The GAUSSIAN16™¶ computational chemistry software package (G16, Rev. A.03) was employed to run quantum mechanical calculations at the MP2/aug-cc-pVTZ and B3LYP-D3(BJ)/Def2TZVP levels. Geometry optimizations were run using the default convergence criteria of G16, and vibrational normal modes calculations allowed to evaluate the Hessian matrix and test the nature of the stationary points. The Natural Bond Orbital (NBO) theory was applied using the 3.1 version of the NBO program implemented in G16. The analysis of the electron density distribution was carried out with the Quantum Theory of Atoms in Molecules (QTAIM) theory,[45] applied through the 3.8 version of the Multiwfn program.[46]

## 4 The AA·$CO_2$ complexes

Theoretical calculations suggest that $CO_2$ binds AA forming a planar six-membered ring characterized by a stronger $OH_{AA}\cdots O_{CO_2}$ hydrogen bond (HB) and a weaker $O_{AA}\cdots C_{CO_2}$ tetrel bond (TB), as in the case of formic acid (FA).[23] In Fig. 1, we also report the intermolecular bond distances, obtained with three different quantum-mechanical approaches: semi-empirical (GFN2-xTB), *ab initio* (MP2/aug-cc-pVTZ), and density functional theory (DFT, B3LYP-D3(BJ)/Def2TZVP), respectively. The predicted HB distances are similar for all methods ($d_{HB}$ = 2.0 Å), whereas the TB distances predicted by the semi-empirical model ($d_{TB}$ = 2.6 Å) are significantly shorter than those obtained with *ab initio* and DFT calculations ($d_{TB}$ = 2.8 Å). Comparing the two conformers, the HB is slightly shorter in *t*AA·$CO_2$ (by about 0.008 Å), whereas the TB is slightly shorter in *c*AA·$CO_2$ (by about 0.006 Å). Despite these differences, the intermolecular binding energy of the two conformers, estimated as the difference between the electronic energy of the complex and the sum of the electronic energy of the single molecules, is basically

¶ Gaussian is a registered trademark of Gaussian, Inc. 340 Quinnipiac St. Bldg. 40 Wallingford, CT 06492, USA.

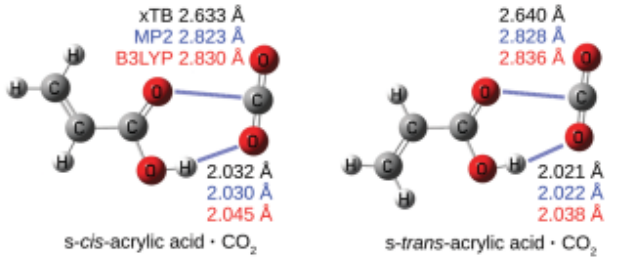


Fig. 1 Observed forms of acrylic acid·$CO_2$: the arrangement is planar and, due to the formation of a HB and a TB, a six membered ring can be recognized. The theoretical intermolecular bond distances are also given: top black values from GFN2-xTB calculations, middle blue values from MP2/aug-cc-pVTZ calculations, bottom red values from B3LYP-D3(BJ)/Def2TZVP calculations.

the same ($D_e \simeq 21$ kJ mol$^{-1}$, see Table 1). As regards the effect of the side chain, comparison with FA·$CO_2$ shows that the HB distance does not change, whereas the TB distance is shortened by about 0.05 Å when the allyl group substitutes the alkyl hydrogen atom. Accordingly, the AA·$CO_2$ intermolecular binding energy is greater than that determined for FA·$CO_2$ ($D_e$ = 19.5 kJ mol$^{-1}$ at the MP2/aug-cc-pVTZ level of calculation[23]) by about 1 kJ mol$^{-1}$.

### 4.1 Rotational spectrum

The accuracy of the employed calculation methods can be verified by the rotational spectroscopy investigation of AA·$CO_2$. Based on the energy and the spectroscopic parameters, reported in Table 1, the rotational spectra of *c*AA·$CO_2$ and *t*AA·$CO_2$ were predicted and used for the spectral analysis. In the recorded spectrum, two sets of transition lines were found, belonging to *c*AA·$CO_2$ and *t*AA·$CO_2$. According to the expected relative abundance ($N_{tAA\cdot CO_2}/N_{cAA\cdot CO_2} \simeq 3/5$ at room temperature) and the values of electric dipole moment components, the spectrum of *c*AA·$CO_2$ was indeed the most intense one. For both conformers, 23 $\mu_a$-type and 11 $\mu_b$-type lines with lower $J$ = 1–8, were observed, whereas no $\mu_c$-type transitions were detected, in agreement with the null value of the $\mu_c$ electric dipole moment component expected for a planar molecular arrangement. The list of the measured transition lines is given in the appendix (Table 4), and the spectroscopic parameters obtained from the analysis of the measured spectra are reported in Table 2. The experimental rotational constants are close both to the *ab initio* and DFT calculations, the differences being within 1.5%, whereas they rise up to 7% for the semi-empirical model ($A$, $B$, $C$ being 4497, 1017, 829 MHz for *c*AA·$CO_2$, and 6251, 914, 797 MHz, for *t*AA·$CO_2$). As a consequence, we can state that for both conformers the observed arrangement is the expected one (the planar six-membered ring formed by the carboxylic group and the $CO_2$, by means of a HB and a TB) and that the semi-empirical model, which provides the shortest TB distances, over-estimates the TB interaction energy.

It is worth noting that the observed inertial defects are $\Delta_0 \simeq -0.5$ uÅ$^2$ for *c*AA·$CO_2$ and $-0.8$ uÅ$^2$ for *t*AA·$CO_2$, while a value close to zero should be expected for a planar structure. Indeed, the inertial defect, defined as:

$$\Delta_0 = \frac{h}{8\pi^2}\cdot\left(-\frac{1}{A}-\frac{1}{B}+\frac{1}{C}\right) = -2\cdot\sum_{i=1}^{\text{atoms}} m_i\cdot c_i^2 \qquad (1)$$

is a descriptor of the displacements of the $m_i$ atomic masses along the *c*-axis, which is perpendicular to the molecular symmetry plane. Values close to zero have been experimentally determined for both *c*AA ($\Delta_0 = -0.037$ uÅ$^2$) and *t*AA ($\Delta_0 = -0.049$ uÅ$^2$)[31] as well as for the FA·$CO_2$ complex ($\Delta_0 = +0.023$ uÅ$^2$).[23] Therefore, it was surprising when we found "large" negative inertial defects for AA·$CO_2$. As discussed by T. Oka in his work dedicated to large negative inertial defects in planar molecules, this suggests an out-of-plane motion taking place within the complex.[47] Therefore, a description of the coupling between the vibrational and rotational motions was attempted *via* the vibrational perturbation theory (VPT2) algorithm,[48] that allows to obtain the vibrational–rotational couplings constants, from which the ground state rotational constants can be obtained, *i.e.*:

$$B_0 = B_e - \frac{1}{2}\cdot\Sigma_i\alpha_i^B \qquad (2)$$

Table 1 Theoretical parameters of s-*cis*-acrylic acid·$CO_2$ and s-*trans*-acrylic acid·$CO_2$, obtained at the B3LYP-D3(BJ)/Def2TZVP and MP2/aug-cc-pVTZ levels of calculation: relative energies, intermolecular binding energies, electric dipole moment components, and rotational constants

| | B3LYP-D3(BJ) | | MP2 | |
|---|---|---|---|---|
| | *c*AA·$CO_2$ | *t*AA·$CO_2$ | *c*AA·$CO_2$ | *t*AA·$CO_2$ |
| $\Delta E_e$ [kJ mol$^{-1}$] | 0[a] | 1.36 | 0[b] | 0.97 |
| $\Delta E_0$ [kJ mol$^{-1}$] | 0[c] | 1.35 | 0[d] | 1.04 |
| $D_e$ [kJ mol$^{-1}$] | 21.2 | 21.2 | 20.7 | 20.7 |
| $D_0$ [kJ mol$^{-1}$] | 18.3 | 18.4 | 17.6 | 17.6 |
| $\mu_a$ [D] | −1.26 | −1.60 | −1.14 | −1.47 |
| $\mu_b$ [D] | 0.62 | 1.12 | 0.53 | 0.99 |
| $\mu_c$ [D] | 0 | 0 | 0 | 0 |
| $\mu_{tot}$ [D] | 1.40 | 1.95 | 1.26 | 1.77 |
| $A$ [MHz] | 4581.313 | 6037.628 | 4531.489 | 5962.647 |
| $B$ [MHz] | 950.021 | 873.713 | 956.221 | 879.240 |
| $C$ [MHz] | 786.853 | 763.261 | 789.602 | 766.250 |

[a] $E_h$ = −455.049723. [b] $E_h$ = −455.972012. [c] $E_h$ = −455.891962. [d] $E_h$ = −454.969671.

Table 2 Experimental rotational and quartic centrifugal distortion constants of s-*cis*-acrylic acid·$CO_2$ and s-*trans*-acrylic acid·$CO_2$

| | *c*AA·$CO_2$ | *t*AA·$CO_2$ |
|---|---|---|
| $A$ [MHz] | 4512.716(5)[a] | 5993.591(5) |
| $B$ [MHz] | 947.7465(5) | 867.8623(5) |
| $C$ [MHz] | 783.9020(4) | 758.9657(5) |
| $D_J$ [kHz] | 0.408(2) | 0.286(2) |
| $D_{JK}$ [kHz] | −1.30(4) | −0.90(4) |
| $D_K$ [kHz] | 9.(1) | 10.(1) |
| $d_1$ [kHz] | −0.086(2) | −0.040(2) |
| $\sigma^b$ [kHz] | 4 | 2 |
| $N^c$ | 34 | 34 |

[a] Error in parentheses in units of the last digit. [b] Root-mean-square deviation of the fit. [c] Number of lines in the fit.

Table 3 Comparison between experimental and calculated (B3LYP-D3(BJ)/Def2TZVP) inertial defects ($\Delta_0$ [uÅ$^2$]) of s-*cis*-acrylic acid·$CO_2$ and s-*trans*-acrylic acid·$CO_2$ and formic acid·$CO_2$

| | *c*AA·$CO_2$ | *t*AA·$CO_2$ | FA·$CO_2$ |
|---|---|---|---|
| Exp. | −0.536 | −0.768 | 0.023[23] |
| Calc. | −0.557 | −0.781 | 0.002 |

Since the computing time required for the derivation of the anharmonic force field is very large, only the DFT method was applied. As can be seen in Table 3, the inertial defects obtained from the ground state rotational constants, reproduce quite well the experimental values of both AA·$CO_2$ complexes and FA·$CO_2$. The analysis of the contribution of the vibrational normal modes shows that all of them contribute to the $\Delta_0$ values. However, the lower energy motions have the largest effect, in particular, the main contribution comes from all the intermolecular motions and the internal torsion of acrylic acid around the C–C single bond.

### 4.2 Intermolecular binding energies

The sums of the van der Waals radii of the atoms involved in the interaction exceed the estimated HB and TB distances by $\delta_{HB}$ = 0.7 and $\delta_{TB}$ = 0.4 Å, respectively, evidencing the strength of the HB with respect to the TB.

To gain insight on their specific contribution, a description in terms of local orbitals was undertaken. The NBO analysis shows that the main contribution to HB is the electron donation from the oxygen lone pairs of $CO_2$ to the σ*(H–O) antibonding orbital of AA, whereas the TB is dominated by the electron donation from the oxygen lone pairs of AA to the π*(O–C) antibonding orbital of $CO_2$. The involved orbitals are shown in Fig. 2 with the related stabilization energy values estimated by the second-order perturbation theory ($E''$). For both HB and TB, two different kinds of lone pairs are involved: one with essential p character (greater $E''$ value) and the other with essential s character (smaller $E''$ value). Overall, the stabilization energy values for TB and HB are $E'' \simeq 7$ kJ mol$^{-1}$ and $E'' \simeq 21$ kJ mol$^{-1}$, respectively, and their ratio is about 1/3.

A different approach involves the analysis of the electron density ($\rho$) distribution, which is expected to be greater along the bonds. In Fig. 3, the plot of two selected electron density contours in the molecular plane obtained at the MP2/aug-cc-pVTZ level of calculation are given. The inner contour encloses all the points with $\rho \geq 0.016$ e Bohr$^{-3}$ and defines a high electron density path between the acidic hydrogen and the $CO_2$ oxygen atom. The outer contour encloses all the points with $\rho \geq 0.009$ e Bohr$^{-3}$, identifying a second high electron density path connecting the AA's carbonyl oxygen and the $CO_2$ carbon atoms. These high electron density paths represent the intermolecular HB and TB, respectively.

In Fig. 3 we also show the $\rho$ gradient trajectories, which, according to the QTAIM theory,[45] allow to partition the molecular space into atom basins (green lines) that are linked together by shared interatomic surfaces and to determine the nuclei as maxima in the electron density space, the bond paths (blue lines) as ridges of high electron density values between

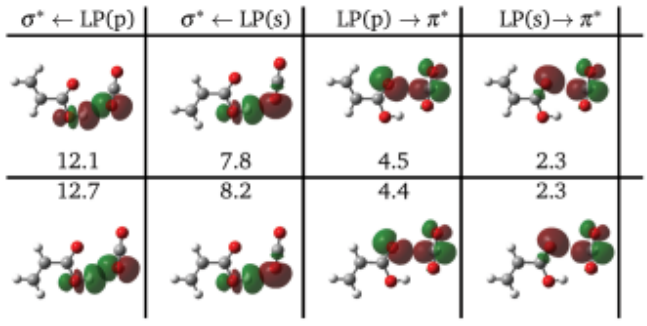


Fig. 2 Theoretical (MP2/aug-cc-pVTZ) natural atomic orbital pairs involved in intermolecular interactions in s-*cis*-acrylic acid·$CO_2$ (top) and s-*trans*-acrylic acid·$CO_2$ (bottom), and corresponding stabilization energy values ($E''$ [kJ mol$^{-1}$]).

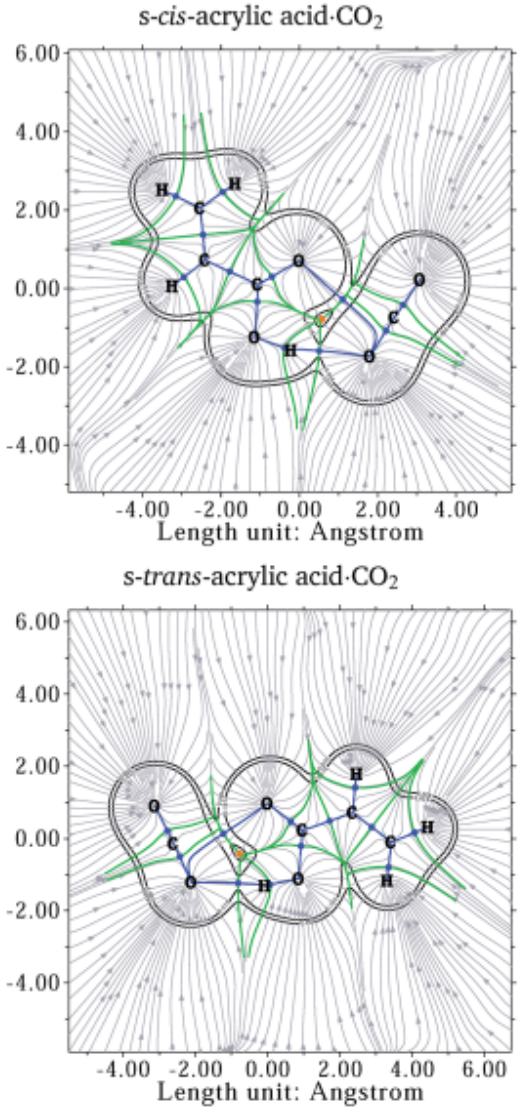


Fig. 3 Gradient trajectories mapped on a total electron density plot (contour levels at $\rho$ = 0.009 and 0.016 e Bohr$^{-3}$) in the molecular plane, showing the atom basins (green lines), bond paths (blue lines), bond critical points (blue), and a ring critical point (orange).

nuclei, and the bond critical points (BCP, blue points) as saddle points lying at the minimum of the bond paths. The electron density values of the BCPs associated to the intermolecular bonds are $\rho_{HB}$ = 0.018 and $\rho_{TB}$ = 0.010 e Bohr$^{-3}$, respectively. Interestingly, the ratio between the shortening of the interatomic distances with respect to the sum of the van der Waals radii of the atoms involved in the interaction ($\delta_{TB}/\delta_{HB}$ = 0.57) and the ratio between the corresponding BCPs electron densities ($\rho_{TB}/\rho_{HB}$ = 0.56) are quite similar.

## 5 The RCOOH·$(CO_2)_{16}$ clusters

When using $scCO_2$ as solvent, because of the high number of $CO_2$ molecules, several competing interactions take place, and it is not a trivial task to understand the driving forces determining the molecular arrangement.

As regards pure $CO_2$ clusters, $(CO_2)_n$, experimental resolved structures have been obtained from the vibra-rotational spectroscopy, for $n$ = 2, 3, 6, and 13. The dimer is planar with $C_{2h}$ symmetry and slipped-parallel structure, stabilized by two C–O intermolecular interactions ($d_{CO}$ = 3.14(3) Å).[49,50] For the trimer, two isomers were observed, one having a planar cyclic structure with $C_{3v}$ symmetry[51–53] and the other a twisted barrel shape with $C_2$ symmetry.[54] In the detected $S_6$ symmetry form of the hexamer, two cyclic $CO_2$ trimers are stacked with coincident symmetry axes but with 'top' and 'bottom' trimers rotated by 60° with respect to one another.[55] In the $(CO_2)_{13}$ cluster, also having a $S_6$ symmetry, a central monomer is enclosed by 12 monomers with carbon atoms located at the vertices of a slightly distorted icosahedron. In general, a compact arrangement of the molecules in the clusters is preferred.

Rotational spectroscopy studies on clusters involving two or three $CO_2$ units and a different molecule are reported for water,[56] hydrogen cyanide,[57] carbonyl sulfide,[58] and fluoroethylene.[59] For OCS·$(CO_2)_2$ a distorted cylinder like motif similar to that of the $C_{2v}$ trimer of $CO_2$ has been determined. In the case of $H_2O$·$(CO_2)_2$[56] and HCN·$(CO_2)_2$,[57] the lone pairs of the heteroatoms are directed toward the carbon atoms of the $CO_2$ units, which in turn are stacked on each other. The HCN·$(CO_2)_3$ tetramer has a $C_3$ symmetry with HCN lying onto the symmetry axis and the nitrogen atom pointing to the center of a $C_{3v}$ cyclic arrangement of $CO_2$ units.[60] In $CH_2$=CHF·$(CO_2)_2$, one of the $CO_2$ units acts as bidentated ligand with the H–C–F or H–C=C–F frames, whereas the other lies above the fluoroethylene plane.[59]

In this work, we try to understand the solvation properties of carboxylic acids by modelling the 1:16 carboxylic acid·$CO_2$ clusters of both FA and AA, using the same theoretical approach as for the 1:1 complexes. The choice of using 16 carbon dioxide units allows the simulation of a nanometric size system and represents a limit for our computational resources. The CREST program was first used for the exploration of the conformational space at the GFN2-xTB level of theory. Several unique aggregates RCOOH·$(CO_2)_{16}$ were found within a 25 kJ mol$^{-1}$ relative energy window. All these structures were then further optimized at the B3LYP-D3(BJ)/Def2-TZVP level of calculation, but due to the slow convergence process, for some of them it has not been possible to reach the minimum energy condition. More specifically, 19 conformers out of 21 were determined for FA·$(CO_2)_{16}$, 34 out of 60 for *c*AA·$(CO_2)_{16}$, and 18 out of 39 for *t*AA·$(CO_2)_{16}$. The corresponding intermolecular binding energy values are summarized in Fig. 4. The values are distributed homogeneously in the range $D_e$ = 265–287 kJ mol$^{-1}$, and a set of 5 isomers for *c*AA·$(CO_2)_{16}$ lie in $D_e$ = 289–293 kJ mol$^{-1}$.

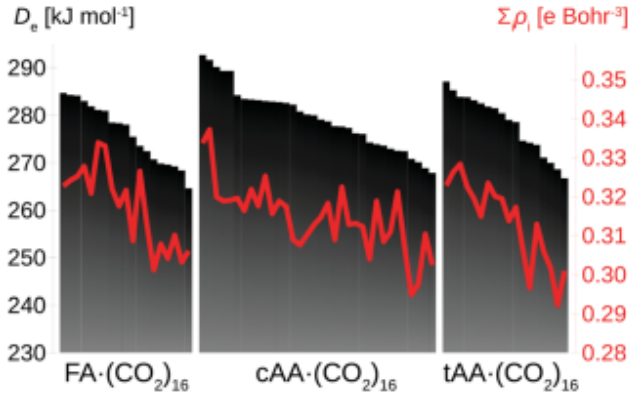


Fig. 4 Cluster binding energy values ($D_e$, black bars), and sum of the electron density values at the bond critical points ($\Sigma_i\rho_i$, red lines) of the R–COOH·$(CO_2)_{16}$ structures optimized at the B3LYP-D3(BJ)/Def2TZVP level of calculation.

For each cluster, a QTAIM analysis[45] was then carried out in order to characterize the intermolecular interactions. Overall, the number of BCPs in each cluster is between 49–59, and the sum of the corresponding electron density values is $\Sigma_i\rho_i$ = 0.292–0.337 e Bohr$^{-3}$. These last values are also reported in Fig. 4 for comparison, where a general conformity between the trends of the total intermolecular binding energy $D_e$ and the total BCPs electron densities $\Sigma_i\rho_i$ can be recognized. Both these descriptors can be related the overall cohesive force of the cluster.

By visual inspection of the optimized nanosolvated structures, we could identify the following common features: (i) a network of TBs is formed among $CO_2$ molecules, and between the oxygen atoms of the acid and the closest $CO_2$ molecules, (ii) the planar six-membered ring characterizing the 1:1 complexes is broken, (iii) non linear HBs take place between the acids and the $CO_2$ molecules closest to the OH group, (iv) the $CO_2$ molecules tend to surround FA, whereas the allyl tail of AA tends to occupy the external part of the cluster, and (v) the clusters have a compact distribution with sizes along the three principal inertia axes of about 1–1.5 nm. As an example, the most stable species for each considered carboxylic acid are shown in Fig. 5 with the cluster sizes, the binding energy values and the HB distances. The corresponding Cartesian structures are also available in the ESI.†

## 6 Conclusions

Two isomers of AA·$CO_2$ were unequivocally identified by pulsed-jet Fourier transform rotational spectroscopy performed

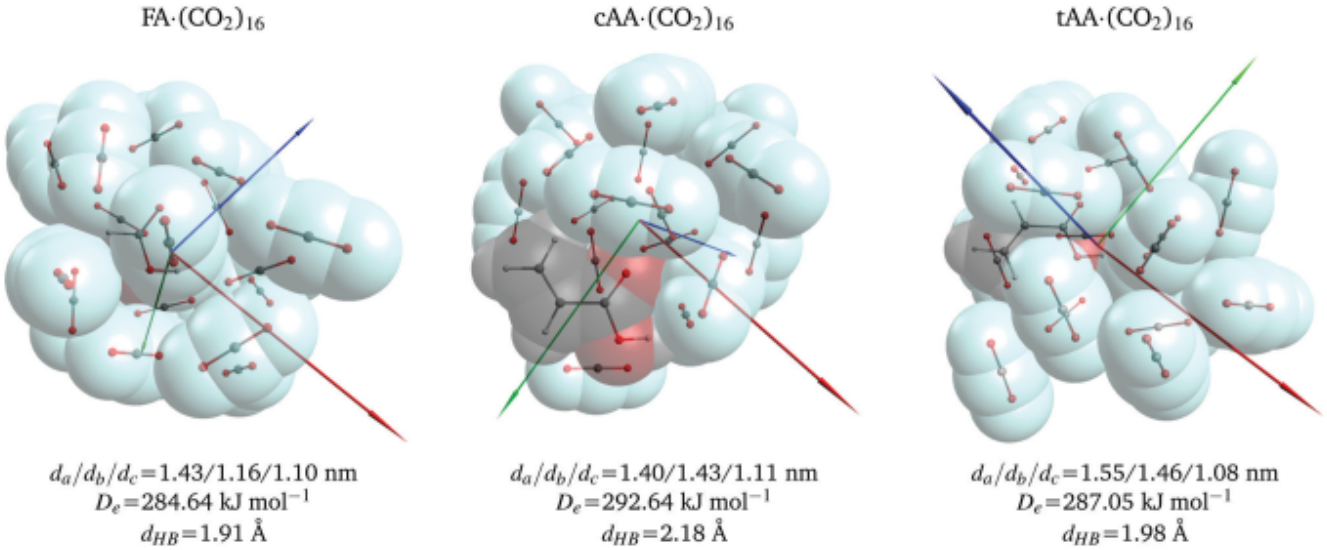


Fig. 5 Combined ball and stick and van der Waals spheres representations of the most stable R−COOH·$(CO_2)_{16}$ cluster structures optimized at the B3LYP-D3(BJ)/Def2TZVP level of calculation. The *a*, *b*, and *c* principal inertial axes are shown as red, green and blue arrows, respectively. Representative parameters are also given: extension along the principal inertial axes, intermolecular binding energy, and hydrogen bond distance.

between 6.5–18.5 GHz. Negative inertial defect values, significantly larger than that found for the similar and previously studied FA·$CO_2$ complex,[23] were explained by accurate quantum mechanical description of the vibrational–rotational coupling interaction. Comparison with experimental data proved that high level DFT and *ab initio* methods fairly reproduce both the HB and TB features, whereas the semi-empirical GFN2-xTB approach over-estimates the strength of the TB. Increasing to 16 the number of $CO_2$ units showed that the carboxylic group can be efficiently solvated by $CO_2$, whereas the allyl chain tends to occupy the outer side of the nanoparticle.

## Conflicts of interest

There are no conflicts to declare.

## Appendix

Table 4 Observed rotational transition frequencies ($\nu$ [MHz]) of s-*cis*-acrylic acid·$CO_2$ and s-*trans*-acrylic acid·$CO_2$

| $J'_{K'_a,K'_c} - J''_{K''_a,K''_c}$ | *c*AA·$CO_2$ | *t*AA·$CO_2$ |
|---|---|---|
| $2_{1,2} - 1_{0,1}$ | | 8270.477 |
| $2_{2,0} - 2_{1,1}$ | 10700.324 | 15378.771 |
| $2_{2,1} - 2_{1,2}$ | 11186.328 | 15703.739 |
| $3_{1,3} - 2_{0,2}$ | 8352.407 | 9734.599 |
| $3_{2,2} - 2_{1,1}$ | 15889.740 | |
| $3_{2,1} - 2_{1,2}$ | 16408.818 | |
| $3_{2,1} - 3_{1,2}$ | 10480.127 | 15223.391 |
| $3_{2,2} - 3_{1,3}$ | 11435.509 | 15868.163 |
| $4_{0,4} - 3_{0,3}$ | 6871.678 | |
| $4_{1,3} - 3_{1,2}$ | 7242.775 | |
| $4_{1,4} - 3_{0,3}$ | 9767.673 | 11147.086 |
| $5_{0,5} - 4_{0,4}$ | 8549.537 | 8099.794 |
| $5_{1,5} - 4_{1,4}$ | 8225.532 | 7854.449 |
| $5_{1,4} - 4_{1,3}$ | 9042.234 | 8398.539 |
| $5_{2,4} - 4_{2,3}$ | 8645.833 | 8130.219 |
| $5_{2,3} - 4_{2,2}$ | 8754.317 | 8164.417 |
| $5_{3,3} - 4_{3,2}$ | 8675.929 | 8139.805 |
| $5_{3,2} - 4_{3,1}$ | 8678.364 | 8140.156 |
| $5_{1,5} - 4_{0,4}$ | 11121.523 | 12511.442 |
| $6_{0,6} - 5_{0,5}$ | 10202.987 | 9701.110 |
| $6_{1,6} - 5_{1,5}$ | 9857.109 | 9420.811 |
| $6_{1,5} - 5_{1,4}$ | 10833.554 | 10073.175 |
| $6_{2,5} - 5_{2,4}$ | 10364.797 | 9753.044 |
| $6_{2,4} - 5_{2,3}$ | 10551.261 | 9812.644 |
| $6_{1,6} - 5_{0,5}$ | 12429.103 | 13832.461 |
| $7_{0,7} - 6_{0,6}$ | 11830.647 | 11292.658 |
| $7_{1,7} - 6_{1,6}$ | 11482.277 | 10984.853 |
| $7_{1,6} - 6_{1,5}$ | 12614.455 | 11744.890 |
| $7_{2,6} - 6_{2,5}$ | 12078.235 | 11374.110 |
| $7_{2,5} - 6_{2,4}$ | 12368.300 | 11468.835 |
| $7_{1,7} - 6_{0,6}$ | | 15116.198 |
| $8_{0,8} - 7_{0,7}$ | 13433.682 | 12873.325 |
| $8_{1,7} - 7_{1,6}$ | | 13413.074 |
| $8_{1,8} - 7_{1,7}$ | 13100.708 | 12546.308 |
| $8_{2,7} - 7_{2,6}$ | | 12993.142 |
| $8_{2,6} - 7_{2,5}$ | | 13133.798 |
| $8_{1,8} - 7_{0,7}$ | 14978.453 | 16369.848 |
| $9_{0,9} - 8_{0,8}$ | 15015.747 | |
| $9_{1,8} - 8_{1,7}$ | 16134.200 | 15077.024 |

## Acknowledgements

This work has been supported by the University of Bologna (RFO), MIUR (FABR), and Fondazione Cassa di Risparmio di Bologna. We acknowledge the CINECA award under the ISCRA initiative for the availability of high performance computing resources. W. L. thanks Prof. T. Oka for the discussion about inertial defect in planar molecules. A. M. thanks Dr A. Acocella for the discussion about NBO theory.

## Notes and references


1 J. Peach and J. Eastoe, *Beilstein J. Org. Chem.*, 2014, **10**, 1446–1460.

2 F. Ingrosso and M. F. Ruiz-López, *Chem. Phys. Chem.*, 2017, **18**, 2560–2572.

3 J. C. M. Pires, F. G. Martins, M. C. M. Alvim-Ferraz and M. Simões, *Chem. Eng. Res. Des.*, 2011, **89**, 1446–1460.

4 M. Becucci and S. Melandri, *Chem. Rev.*, 2016, **116**, 5014–5037.

5 F. Baiocchi, T. Dixon, C. Joyner and W. Klemperer, *J. Chem. Phys.*, 1981, **74**, 6544–6549.

6 R. Altman, M. D. Marshall and W. Klemperer, *J. Chem. Phys.*, 1982, **77**, 4344–4349.

7 K. I. Peterson and W. Klemperer, *J. Chem. Phys.*, 1984, **80**, 2439–2445.

8 J. Rice, F. Lovas, G. Fraser and R. Suenram, *J. Chem. Phys.*, 1995, **103**, 3877–3884.

9 J. J. Newby, R. A. Peebles and S. A. Peebles, *J. Phys. Chem. A*, 2004, **108**, 11234–11240.

10 D. J. Frohman, E. S. Contreras, R. S. Firestone, S. E. Novick and W. Klemperer, *J. Chem. Phys.*, 2010, **1332**(1–6), 244303.

11 J. Doran, B. Hon and K. Leopold, *J. Mol. Struct.*, 2012, **1019**, 191–195.

12 L. Kang, P. Davis, I. Dorell, K. Li, O. Oncer, L. Wang, S. E. Novick and S. G. Kukolich, *J. Mol. Spectrosc.*, 2017, **342**, 62–72.

13 T. D. Klots, R. S. Ruoff and H. S. Gutowsky, *J. Chem. Phys.*, 1989, **90**, 4216–4221.

14 K. R. Leopold, G. T. Fraser and W. Klemperer, *J. Chem. Phys.*, 1984, **80**, 1039–1046.

15 K. I. Peterson, R. D. Suenram and F. J. Lovas, *J. Chem. Phys.*, 1991, **94**, 106–117.

16 G. Sedo and J. van Wijngaarden, *J. Chem. Phys.*, 2009, **131**(1–5), 044303.

17 S. E. Novick, R. D. Suenram and F. J. Lovas, *J. Chem. Phys.*, 1988, **88**, 687–690.

18 T. Blake and S. Novick, *J. Mol. Spectrosc.*, 1992, **154**, 72–82.

19 V. Ilyushin, F. Lovas and D. Plusquellic, *J. Mol. Spectrosc.*, 2006, **239**, 94–100.

20 Y. Orita, Y. Kawashima and E. Hirota, *J. Mol. Spectrosc.*, 2011, **268**, 78–84.

21 Y. Kawashima, A. Sato, Y. Orita and E. Hirota, *J. Phys. Chem. A*, 2012, **116**, 1224–1236.

22 A. J. Thomas, M. M. Serafin, A. A. Ernst, R. A. Peebles and S. A. Peebles, *J. Mol. Spectrosc.*, 2013, **289**, 65–73.

23 A. Vigorito, Q. Gou, C. Calabrese, S. Melandri, A. Maris and W. Caminati, *Chem. Phys. Chem.*, 2015, **16**, 2961–2967.

24 A. M. Anderton, R. A. Peebles and S. A. Peebles, *J. Phys. Chem. A*, 2016, **120**, 247–253.

25 R. E. Dorris, W. C. Trendell, R. A. Peebles and S. A. Peebles, *J. Phys. Chem. A*, 2016, **120**, 7865–7872.

26 S. Gao, D. A. Obenchain, J. Lei, G. Feng, S. Herbers, Q. Gou and J. U. Grabow, *Phys. Chem. Chem. Phys.*, 2019, **21**, 7016–7020.

27 T. Lu, J. Zhang, Q. Gou and G. Feng, *Phys. Chem. Chem. Phys.*, 2020, **22**, 8467–8475.

28 W. Cheng, Y. Zheng, S. Herbers, H. Zheng and Q. Gou, *Chem. Phys. Chem.*, 2021, **22**, 154–159.

29 Y. Zheng, S. Herbers, Q. Gou, W. Caminati and J.-U. Grabow, *J. Phys. Chem. Lett.*, 2021, **12**, 3907–3913.

30 K. Bolton, D. Lister and J. Sheridan, *J. Chem. Soc., Faraday Trans.*, 1974, **70**, 113–123.

31 C. Calabrese, A. Vigorito, G. Feng, L. Favero, A. Maris, S. Melandri, W. Geppert and W. Caminati, *J. Mol. Spectrosc.*, 2014, **295**, 37–43.

32 C. Calabrese, A. Maris, L. Dore, W. Geppert, P. Fathi and S. Melandri, *Mol. Phys.*, 2015, **113**, 2290–2295.

33 G. Feng, L. Favero, A. Maris, A. Vigorito, W. Caminati and R. Meyer, *J. Am. Chem. Soc.*, 2012, **134**, 19281–19286.

34 G. Feng, Q. Gou, L. Evangelisti and W. Caminati, *Angew. Chem., Int. Ed.*, 2014, **53**, 530–534.

35 G. Feng, Q. Gou, L. Evangelisti, Z. Xia and W. Caminati, *Phys. Chem. Chem. Phys.*, 2013, **15**, 2917–2922.

36 Q. Gou, G. Feng, L. Evangelisti and W. Caminati, *J. Phys. Chem. A*, 2013, **117**, 13500–13503.

37 Q. Gou, G. Feng, L. Evangelisti and W. Caminati, *J. Phys. Chem. Lett.*, 2013, **4**, 2838–2842.

38 J.-U. Grabow, W. Stahl and H. Dreizler, *Rev. Sci. Instrum.*, 1996, **67**, 4072–4084.

39 T. Balle and W. Flygare, *Rev. Sci. Instrum.*, 1981, **52**, 33–45.

40 W. Caminati, L. Evangelisti, G. Feng, B. Giuliano, Q. Gou, S. Melandri and J.-U. Grabow, *Phys. Chem. Chem. Phys.*, 2016, **18**, 17851–17855.

41 H. Pickett, *J. Mol. Spectrosc.*, 1991, **148**, 371–377.

42 J. Watson, *Vibrational Spectra and Structure*, Elsevier, New-York/Amsterdam, 1977.

43 P. Pracht, F. Bohle and S. Grimme, *Phys. Chem. Chem. Phys.*, 2020, **22**, 7169–7192.

44 C. Bannwarth, E. Caldeweyher, S. Ehlert, A. Hansen, P. Pracht, J. Seibert, S. Spicher and S. Grimme, *Wiley Interdiscip. Rev.: Comput. Mol. Sci.*, 2021, **11**(1–49), e1493.

45 R. F. W. Bader, *Atoms in Molecules: a Quantum Theory*, Oxford University Press, 1990.

46 F. Lu and T. Chen, *J. Comput. Chem.*, 2012, **33**, 580–592.

47 T. Oka, *J. Mol. Struct.*, 1995, **352/353**, 553–566.

48 J. Bloino and V. Barone, *J. Chem. Phys.*, 2012, **136**(1–15), 124108.

49 M. Walsh, T. England, T. Dyke and B. Howard, *Chem. Phys. Lett.*, 1987, **142**, 265–270.

50 K. W. Jucks, Z. S. Huang, R. E. Miller, G. T. Fraser, A. S. Pine and W. J. Lafferty, *J. Chem. Phys.*, 1988, **88**, 2185–2195.

51 G. T. Fraser, A. S. Pine, W. J. Lafferty and R. E. Miller, *J. Chem. Phys.*, 1987, **87**, 1502–1508.

52 M. J. Weida, J. M. Sperhac and D. J. Nesbitt, *J. Chem. Phys.*, 1995, **103**, 7685–7699.

53 M. Dehghany, M. Afshari, N. Moazzen-Ahmadi and A. R. W. McKellar, *J. Chem. Phys.*, 2008, **128**(1–5), 064308.

54 M. J. Weida and D. J. Nesbitt, *J. Chem. Phys.*, 1996, **105**, 10210–10223.

55 J. Norooz Oliaee, M. Dehghany, N. Moazzen-Ahmadi and A. R. W. McKellar, *Phys. Chem. Chem. Phys.*, 2011, **13**, 1297–1300.
56 K. I. Peterson, R. D. Suenram and F. J. Lovas, *J. Chem. Phys.*, 1989, **90**, 5964–5970.
57 H. S. Gutowsky, J. Chen, P. J. Hajduk and R. S. Ruoff, *J. Phys. Chem.*, 1998, **94**, 7774–7780.
58 S. A. Peebles and R. L. Kuczkowski, *J. Chem. Phys.*, 1998, **109**, 5276–5282.
59 P. B. Kannangara, C. T. West, S. A. Peebles and R. A. Peebles, *Chem. Phys. Lett.*, 2018, **706**, 538–542.
60 H. S. Gutowsky, P. J. Hajduk, C. Chuang and R. S. Ruoff, *J. Chem. Phys.*, 1990, **92**, 862–869.